Particle-in-cell modeling of magnetized argon plasma flow through small mechanical apertures

Adam B. Sefkow[1] and Samuel A. Cohen[2]
[1]*Sandia National Laboratories, P.O. Box 5800, Albuquerque, New Mexico 87185, USA*
[2]*Princeton Plasma Physics Laboratory, P.O. Box 451, Princeton, New Jersey 08543, USA*

(Received 24 February 2009; accepted 26 March 2009; published online 1 May 2009)

Motivated by observations of supersonic argon-ion flow generated by linear helicon-heated plasma devices, a three-dimensional particle-in-cell (PIC) code is used to study whether stationary electrostatic layers form near mechanical apertures intersecting the flow of magnetized plasma. By self-consistently evaluating the temporal evolution of the plasma in the vicinity of the aperture, the PIC simulations characterize the roles of the imposed aperture and applied magnetic field on ion acceleration. The PIC model includes ionization of a background neutral-argon population by thermal and superthermal electrons, the latter found upstream of the aperture. Near the aperture, a transition from a collisional to a collisionless regime occurs. Perturbations of density and potential, with millimeter wavelengths and consistent with ion acoustic waves, propagate axially. An ion acceleration region of length $\sim 200\lambda_{D,e}-300\lambda_{D,e}$ forms at the location of the aperture and is found to be an electrostatic double layer, with axially separated regions of net positive and negative charge. Reducing the aperture diameter or increasing its length increases the double layer strength. © *2009 American Institute of Physics*. [DOI: 10.1063/1.3119902]

I. INTRODUCTION

Several helicon plasma devices,[1–4] used in studies of warm low-β plasma flow along expanding magnetic fields, have shown the acceleration of plasma to supersonic speeds occurring in short distances, i.e., ~ 50 Debye lengths, $\lambda_{D,e}$, after the field has expanded 10%–20%. Theoretical analyses of these results[5–8] have attributed the ion acceleration to electrostatic layers, single or double, generated by the expanding magnetic field. The Magnetic Nozzle Experiment (MNX) provides, by means of its flexible magnetic and mechanical geometries, a unique database and counterexample to the above statement because, in MNX, the short acceleration region primarily occurs near mechanical apertures intersecting the plasma flow regardless of whether these are located in a converging, constant, or diverging magnetic field region. We show that this fact is due to the presence of an aperture whose size is comparable to or smaller than the ion gyroradius and larger than the electron gyroradius. Explaining these observations will aid in the understanding of the dynamics of plasma acceleration near magnetic nozzles and mechanical apertures and the formation of supersonic collimated jets. MNX experimental results and their interpretation can assist in the development of applications such as plasma propulsion, e.g., the variable specific impulse magnetoplasma rocket (VASIMR),[3] materials processing, and fusion divertors, particularly for linear devices.

The formation and steady-state sustainment of an electrostatic double layer (DL) (distinct regions of net positive and negative charges) are found in simulations of the MNX device we report herein. The DL is the source of the supersonic ion beam in the expansion region (ER). A schematic of MNX is shown in Fig. 1.[1] A pair of large bore (25 cm i.d.) coils in a near Helmholtz configuration provides the primary magnetic field of 20–2000 G at its center. A small bore (1.2 cm i.d.) coaxial coil lies at one end; it is called the nozzle coil and can add another 2500 G at its center. At the opposite end of the machine is a double-saddle helicon antenna outside a 25 cm long Pyrex pipe (5 cm i.d.). This antenna provides about 500 W of rf heating at 27 MHz. The argon plasma about 30 cm downstream from the antenna has a density of $n_p \sim 10^{13}$ cm^{-3}, a bulk electron temperature near $T_e \sim 5$ eV, and a tail temperature near 30 eV. The tail contains about 1% of the density.[9] This plasma flows toward mechanical apertures of varying sizes, from 1–10 mm diameter, and varying axial positions, marked *a*, *b*, *c*, and *d* in Fig. 1. (Usually only one aperture is in place during an experiment.) As shown, apertures have been placed in the center of the Helmholtz coil pair, position *a*, where the field is uniform, and on either side of the nozzle coil, where the field is either diverging or converging. All positions have shown, under similar conditions of field, helicon power, and gas pressure, ion acceleration to supersonic speed in short distances (2–5 mm).[9] Because of the similarity of these results, this paper concentrates on only one configuration, with the aperture placed at position *c*, corresponding to a region in which the field first converges then diverges.

The outline of this paper is as follows. The particle-in-cell (PIC) simulation set up and initialization are described in Sec. II. Section III presents the steady-state plasma flow parameters achieved in the nominal simulation and reveals the presence of an electrostatic DL located within the aperture region. The existence of a high-energy tail in the electron energy distribution function (EEDF) is shown. Section IV investigates variations in the nominal simulated MNX parameters and their influences on DL strength and ion acceleration. A general discussion of the inferred mechanisms involved in the formation of double layers in the MNX device is provided in Sec. V. A summary of important results pertaining to the MNX simulations and the conclusions drawn from them are given in Sec. VI.

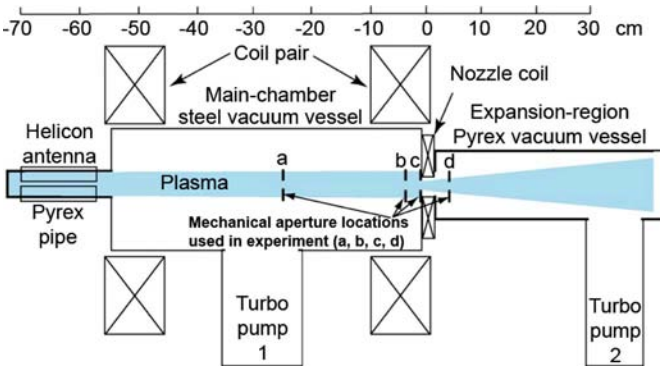

FIG. 1. (Color online) Schematic of the MNX device. A 25 cm bore coil pair forms a Helmholtz-like field. Argon plasma is formed inside the main vacuum chamber (MC) by absorption of helicon waves launched by the antenna at the left. The plasma flows to the right, passing though an aperture and a smaller bore nozzle coil. The aperture may be placed at one of several positions, labeled *a-d*. The vacuum vessel to the right of the nozzle coil is a Pyrex pipe termed the expansion region (ER). The gas pressure is about 0.4–2 mT in the MC and about ten times lower in the ER.

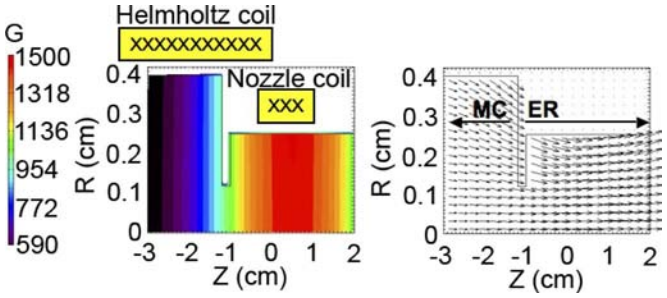

FIG. 2. (Color online) Initialized PIC simulation geometry and magnetic field topology. For the nominal case of peak field strength B_z=1500 G within the nozzle, magnetic field magnitude (left) and vector plot (right) are shown. Ar^+ plasma is injected from the MC on the left and enters the ER, after passing through a mechanical aperture at z=−1.2 cm.

II. SIMULATION SETUP

PIC simulations[10] using the commercial LSP code[11,12] are employed to self-consistently model the plasma dynamics and formation of the electrostatic layer measured in the MNX (Ref. 9) near the mechanical aperture. Argon plasma is formed upstream, in the MNX main chamber (MC), by absorption of helicon waves. The helicon waves and helicon-induced breakdown of the neutral Ar^0 gas are not included in the PIC model at this time. Modeling the entire MNX device is presently too computationally demanding; therefore only a small volume in the vicinity of the magnetic nozzle and aperture is simulated in three-dimensional (3D) $\{r,\theta,z\}$ cylindrical geometry, which extends a few centimeters upstream into the MC and downstream into the ER. Although the simulations are conducted in three dimensions, the results presented herein will be shown as two-dimensional (2D) $\{r,z\}$ contours in the θ=0 plane; analysis and discussion of most 3D effects are left for future publications.

The spatial extent of the particle simulation is $r=\{0,0.42\}$ cm, $\theta=\{0,2\pi\}$, and $z=\{-3,+2\}$ cm, with grid spacings of Δr=0.01 cm, $\Delta\theta=\pi/2$, and Δz=0.05 cm. The $\Delta\theta$ spacing is approximately the minimum resolution of the azimuthal direction allowed by the 3D field solver. Figure 2 provides a representation of the geometry and magnetic field topology. The applied magnetic fields of the Helmholtz and nozzle coils are modeled in the LSP code using a finite-length solenoid sixth-order power series expansion.[13] The lengths, radii, and relative placement of the coils produce a field topology in agreement with a previous independent calculation of the $B_z(z)$ at r=0. The center of the nozzle coil is approximately located at z=0.5 cm, and the peak field used in this nominal simulation is B_z=1500 G at that location. The aperture is within the overlapping fields of the coils about 1.5 cm upstream of the nozzle coil. Therefore, the field is converging and increasing from the MC into the ER, such that the plasma is compressing near the aperture. The field begins to diverge downstream of the center of the nozzle coil, about 1.5 cm beyond the aperture, and decreases by about 33% in the last 1.5 cm of the simulation space.

The aperture itself is chosen to have a nominal inner radius of r_{ap}=0.12 cm and axial length z_{ap}=0.2 cm, from z=−1.2 cm to z=−1 cm. The wall radius is r_{wall}=0.4 cm in the MC and 0.25 cm in the ER. These values were chosen for computational expediency in order to minimize the volume required while still modeling the essential physics since magnetized plasma tied to a field line above a certain radius is lost to the aperture wall at z=−1.2 cm and $r>0.12$ cm; simulations with the same geometry except for larger wall radii demonstrated equivalent results. Whether the radial boundaries of the simulation are modeled as floating conductors or insulators, consistent steady-state behavior is observed with minor differences in the plasma profiles. All results herein use electrically connected conducting walls that are floating and are not grounded or biased. In this model, secondary electron emission is neglected, and particles striking boundaries are removed from the simulation. (The latter ignores locally sourced neutrals, a valid assumption since the mean free path for ionization is longer than 10 cm.) When secondary emission models are included, the overall dynamics again remain approximately the same and so are not reported here. As noted earlier, this is just one of many possible magnetic nozzle and aperture arrangements.[9]

The plasma flow into the system and its subsequent evolution into an equilibrium are self-consistently calculated using traditional PIC methods in the LSP code, including an explicit particle-pushing routine that conserves energy (and is not susceptible to the so-called Debye length numerical instability), a temporally implicit noniterative "unconditionally stable" electromagnetic field solver,[14] and a cloud-in-cell linear interpolation technique between particle locations and grid boundaries. The aspect ratios of the grid spacings are allowed to be relatively large because the electromagnetic fields are solved implicitly. Approximately 12 and 36 particles per cell are adaptively maintained[15] for the Ar^+ and e^- particles (both injected and ionized species), respectively.

Plasma composed of Ar^+ and e^- particles is constantly injected at the upstream end of the MC, fills the chamber, and achieves a steady-state flow after a time $t>10$ μs. Experiments on the MNX demonstrated that the on-axis presheath due to the presence of the aperture wall extends a

few centimeters upstream into the MC, within which the Ar^+ are accelerated into an ion beam, roughly defined as when the average axially directed energy E_i is several times T_i. Therefore, the simulated Ar^+ is injected for all r near the $z=-3$ cm plane in the $+\hat{z}$ direction with a radially constant $E_i \sim 1.5$ eV (i.e., subsonic with $\beta \equiv v_i/c \sim 10^{-5}$) and Maxwellian energy distribution with $T_i \sim 0.3$ eV, within the measured range of E_i and T_i in the presheath in the MC. Since the ion particles are injected as a beam and not thermally, almost all of them have $+v_z\hat{z}$ velocities at $t=0$ and few travel upstream. The initialized axial current density of the ions is a radially constant $J_z \sim 0.13$ A cm^{-2}, which corresponds to an approximate plasma density in the MC of $n_p \sim 3 \times 10^{12}$ cm^{-3}. The electrons are initialized with the same radially constant J_z and drift velocity (for overall charge and current neutrality) and are initially prescribed a Maxwellian energy distribution with $T_e \sim 10$ eV near the boundary. However, dynamic effects, such as plasma density buildup and expansion into the MC and ER, particle losses to boundaries, collisions, and ionization of background neutrals, result in a reduced steady-state average $T_e \sim 5$ eV for $r < r_{ap}$, within the measured range of T_e in the MC ($\sim 2-10$ eV). The plasma located at $r > r_{ap}$ in the MC has a slightly cooler bulk T_e in steady-state equilibrium, since it interacts with the aperture wall. Typical MNX plasma densities in the MC are between 10^{12} and 5×10^{13} cm^{-3}; however, the explicit time step limitation requiring $\Delta t < \omega_{p,e}^{-1}$ ($\sim 10^{-11}-10^{-12}$ s) provides a stringent constraint on the simulations, since a few dozen microseconds need to be simulated (few 10^6-10^7 time steps, with approximately 2×10^6 total particles). A typical simulation runtime is ~ 10 days on 32 processors.

The Ar^+ MNX plasma is partially ($\sim 5\%-50\%$) ionized. Hence, a background neutral Ar^0 population is included and allowed to interact with the injected plasma via scattering and ionization models. The Ar^0 pressure is initialized at a constant ~ 0.75 mTorr ($n_{Ar^0} \sim 2.6 \times 10^{13}$ cm^{-3}) in the MC and linearly decreases from $z=-1.2$ to -1 cm to a constant ER value of ~ 0.2 mTorr ($n_{Ar^0} \sim 7 \times 10^{12}$ cm^{-3}), in reasonable agreement with experimental conditions. Charged particle collisions are treated using internally calculated Spitzer rates, whereas charged-neutral collisions are handled with a Monte Carlo method utilizing energy-dependent user-specified tabular cross sections. Standard elastic scattering and ionization cross sections for e^- on Ar^0 from the literature are employed, whereas Ar^+ on Ar^0 elastic scattering is assigned an energy-independent 10^{-16} cm^{-2} cross section. Neutral-neutral collisions are treated using hard sphere collision rates. Ionization of the Ar^0 by Ar^+ impact is neglected.

III. STEADY-STATE PLASMA AND DOUBLE LAYER PROFILES

Steady-state plasma profiles in the MNX simulations are typically reached after an elapsed time of $t \sim 12 \pm 2$ μs, where $t=0$ signifies the beginning of particle injection from the $-z$ boundary. The approximate time needed to establish steady-state conditions is comparable to the transit time across the simulation space of an argon particle traveling near the sound speed $[C_s \equiv \sqrt{(T_e+3T_i)/m_i}]$. Later we show that the argon particles travel at velocities slightly below C_s in the MC and considerably above C_s throughout the ER.

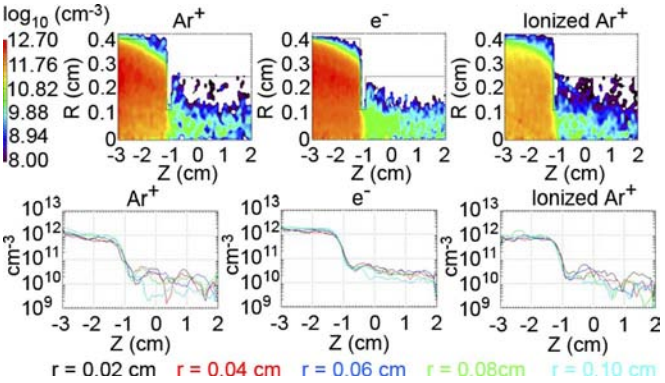

FIG. 3. (Color online) Steady-state density profiles of Ar^+ (left), e^- (middle), and ionized Ar^+ (right), presented as $\{r,z\}$ contours (top) and axial slices through values of $r < r_{ap}$ (bottom). All plots are on a $\log_{10}$ scale. Note the dip in density near $z \sim -0.9$ cm to $z \sim -0.6$ cm, which indicates the presence of a double layer rather than a single layer.

The density profiles of the injected and ionized species are presented in Fig. 3 as $\{r,z\}$ contours and axial slices. When both an applied magnetic field topology and the aperture are used, a significant axial density drop near the aperture self-consistently evolves and is maintained by the constant influx of plasma from the MC boundary. The plasma density drops by more than an order of magnitude and is accompanied by an electrostatic potential drop and sharp increase in $+\hat{z}$-directed average ion energy E_i. The drops are established early in time, essentially as soon as the initial plasma expansion enters the aperture. To be shown later, the change in potential and rapid ion acceleration near the aperture is caused by a static electric field $E_z(z)$, which is established due to the axial separation of two oppositely charged layers, called an electrostatic DL. For the parameters mentioned earlier, the DL approximately exists within the aperture and has a length of $\sim 0.3-0.45$ cm $\sim 200\lambda_{D,e}-300\lambda_{D,e}$, where the electron Debye length $\lambda_{D,e} \propto \sqrt{T_e/n_e}$ references the electron temperature T_e and density n_e values just upstream of the aperture ($\lambda_{D,e}$ is about three to five times longer when evaluated with the downstream plasma parameters). Note that the plasma Debye lengths are not generally resolved by the numerical PIC grid; however, the energy-conserving particle push ensures that spurious numerical heating (normally caused by under-resolving $\lambda_{D,e}$) does *not* occur.

The double layer does not develop in simulations employing the same magnetic field topology without an aperture (even though the field both converges and diverges in separate locations) or when utilizing an aperture without an applied magnetic field. Also, the imposed field needs to be qualitatively similar, i.e., mostly perpendicular to the aperture wall, to the general setup described here. A DL does develop without the neutral population (since plasma is artificially injected from the boundary), which nominally provides scattering and ionization. The formation of the DL in simulations relies upon both an applied magnetic field and a mechanical aperture through which the plasma must pass.

Intriguingly, the PIC simulation for this initialization

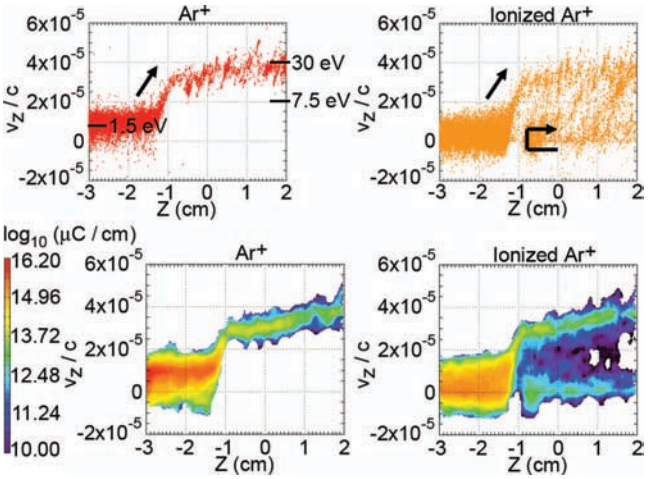

FIG. 4. (Color) Steady-state $\{z,v_z\}$ phase space profiles of Ar^+ (left) and ionized Ar^+ (right) over all z for $r<r_{ap}$, presented as particle plots (top) and charge density contours (bottom) on a $\log_{10}$ scale. Three reference energy values are marked and arrows indicate the DL's role on ion dynamics. The ionized Ar^+ has a two-component distribution in the ER.

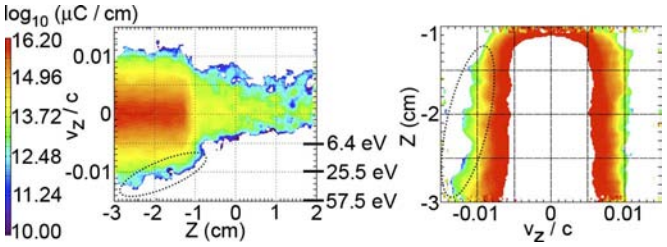

FIG. 5. (Color online) Steady-state $\{z,v_z\}$ phase space profile of the electrons, presented as a charge density contour for $r<r_{ap}$ over all z (left) and for $z<-1.0$ cm in the MC (right) on a $\log_{10}$ scale. The plot on the right has been rotated and rescaled for clarity. Three reference energy values are marked. Ellipses highlight the DL's role on electron dynamics.

scenario predicts an on-axis n_p dip in the MC, witnessed in the $n_p(r)$ profiles near the $r=0$ axis separately for all species. The densities are typically found to be maximum around $r=0.3$ cm, with ratios satisfying $n_p(r=0.3\ \text{cm})/n_p(r=0) \sim 2-3$, accompanied by an on-axis temperature peak such that $P(r)\sim n(r)T(r)$ is approximately constant for each axial location z. In the MNX, helicon wave absorption is estimated to occur over a long distance, about 30 cm. The somewhat higher experimentally achieved n_p may alter the physics compared to these results, which rely upon radially constant injected profiles without helicon waves. Further investigation is needed to determine under what circumstances a density dip (of this small radial extent) can be produced, measured, and understood in the MNX device. One might expect the off-axis plasma, which is almost entirely lost to the aperture wall along field lines for $r>r_{ap}$, to have a relatively cooler electron temperature (smaller $T_{e,\|}$ relative to the field) due to the loss of higher energy electrons to that wall. Reflection of lower energy electrons from the aperture sheath may be the cause of the distribution in the MC being weighted toward lower energies for $r>r_{ap}$. Therefore, the density dip could be a consequence of equilibrium radial pressure balance in the presence of the magnetic field, and the fact that ion gyroradii are comparable in size to the density dip and aperture radius r_{ap}. The small density dip could also be a numerical artifact related to particle noise effects near the $r=0$ singularity.

An electrostatic DL is responsible for accelerating ions from the high potential region (the MC) into the low potential region (the ER) and for accelerating electrons in the opposite manner. Steady-state $\{z,v_z\}$ phase space profiles of the ion species are provided in Fig. 4, in the form of particle plots and density contours. The latter resembles one-dimensional simulations of ion beam formation from a DL within a *diverging* magnetic field reported in Ref. 5, as well as laser-induced fluorescence (LIF) measurements of the same reported in Ref. 16. The figure expectedly demonstrates that any upstream-moving $(-v_z\hat{z})$ ionized Ar^+ particles born in the ER are subsequently reflected from the DL region and back into the ER $(+v_z\hat{z})$ because they lack the necessary energy to cross the potential barrier. Therefore, the ionized Ar^+ population has a two-component distribution in the ER (1) due to particles born in the MC and accelerated across the DL into the ER and (2) from low-energy particles born in the ER and reflected away from the DL. The upstream ionized Ar^+ particles have a slightly broader velocity distribution and slightly slower z-directed flow than the injected Ar^+. The ion velocity in the ER shows coherent ~20% variations with a periodicity of ~0.3 mm, which propagate at approximately the ion sound speed. This length is similar to the length of the DL, a coincidence noted by earlier researchers.[17]

The steady-state $\{z,v_z\}$ phase space profile of the electrons is provided in Fig. 5. The ellipses in that figure emphasize that the $-v_z\hat{z}$ region of the distribution in the MC contains more high-energy electrons compared to those in the $+v_z\hat{z}$ region due to the electrons that are accelerated into the main chamber across the DL from the ER. Those lower energy electrons that are reflected by the DL as they approach it from the MC side are harder to see on these plots, although it is apparent that the $+v_z\hat{z}$ electron distribution has a smaller range in the ER compared to the MC due to deceleration.

The steady-state temperature profiles of the charged-particle species are displayed in Fig. 6. In the LSP code, temperature is a cell quantity defined as $kT=2/3\ E_{ave}$, which averages both the parallel and perpendicular temperatures after subtracting the directed energy. Such a temperature estimate is only an approximation for non-Maxwellian, anisotropic, or magnetized plasma (or for the two-component distribution of the ionized Ar^+ in the ER, as shown in Fig. 4). The "temperature" plots in Fig. 6 do give an illustrative indication of the energy distribution. For example, the plots reveal that the DL separates two sets of distributions with different injected and ionized populations found in each chamber. Potentials are known to develop when plasmas of different properties come into contact.[17]

The electrostatic DL begins to form early in time, as plasma initially flows through the mechanical aperture. The DL strength grows, the relative plasma density and potential drops increase, and the plasma continues to fill the MC and ER until steady-state conditions are reached. As displayed in Fig. 7, the DL manifests in charge density plots as a layer of excess positive charge ρ^+, followed shortly downstream in z by a layer of excess negative charge ρ^-. The static axial

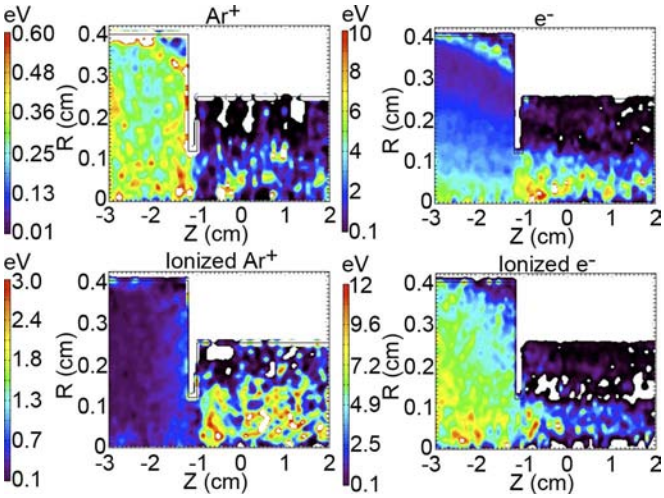

FIG. 6. (Color online) Steady-state temperature profiles of Ar^+ (top left), e^- (top right), ionized Ar^+ (bottom left), and ionized e^- (bottom right), presented as $\{r,z\}$ contours. Temperature is a cell quantity defined as $kT = 2/3\ E_{ave}$ in the LSP code.

electric field E_z, radial electric field E_r, and electrostatic potential ϕ (from integration of the electric field) are also shown in Fig. 7 as both $\{r,z\}$ contour plots and as radially averaged (from $r=0.01$ cm to $r=0.11$ cm) axial slices. The static axial electric field E_z signal caused by the charge separation is clear. Due to interference caused by coherent short-wavelength electrostatic ($k \| E_z$) waves and numerical particle noise, the data presented in Fig. 7 have been averaged in θ as well as time (in steady state, over $\Delta t \sim +3\ \mu$s). The data in Fig. 7 also correspond to a lower (by ~ 0.1) plasma density n_p case than mentioned in Sec. II in order to more clearly highlight the static DL signals above the coherent electrostatic waves and incoherent particle noise.

The strong waves just mentioned are coherent and evident during steady-state plasma flow in the E_z plot of Fig. 8, whose data originate from the nominal simulation parameters previously discussed in Sec. II. The waves cause significant fluctuations to the charge density, electric field, and potential signals of the DL, and their wavelength is modestly resolved by the grid ($\lambda \sim 6\Delta z$). A strong $+E_z$ sheath field exists near the aperture wall at $z=-1.2$ cm for $r > r_{ap}$ (in both Figs. 7 and 8). The larger volumetric proportion of plasma in the MC is lost to that wall, as compared to the amount passing into the ER or striking the radial boundary of the aperture; the $+E_r$ field present within the aperture increases radial ion losses to its wall between $z=-1.2$ and -1 cm at $r=r_{ap}$.

A preliminary analysis indicates that the frequency and wavelength of the coherent E_z modulation roughly correspond to the ion acoustic wave (IAW) mode, which involves both electron and ion motion along (or in the absence of) a magnetic field; coherent ion participation in wave motion is witnessed within the particle plots of Fig. 4. IAWs with phase velocity $\omega/k = v_{ph} \sim C_s$ can exist[18] when $k\lambda_{D,e} \ll 1$ and $v_{th,i} < v_{ph} < v_{th,e}$, both of which are generally satisfied in MNX. When the electrons carry a current, as they do here, the IAW can be destabilized and grow in amplitude when the average electron velocity $v_e > C_s$ (which will be shown to be satisfied near the aperture and in the ER). Anomalous resistivity generated by the IAW instability has been cited as the cause of DL formation in sufficiently long systems involving a buildup of potential.[19] In the limit of $T_i/T_e \ll 1$, the IAW is subject to only weak Landau damping, but this ratio can increase to $T_i/T_e \sim 0.05-0.15$ in the MC near the aperture and in the ER. Wave energy supplied to the ions from Landau damping might be replenished by electron current-driven IAW instability. The presence of the wave is quite robust and not consistent with PIC noise, as it persists with defined and propagating amplitudes under a variety of circumstances (changes in grid sizes, particle counts, dimensions, etc.).

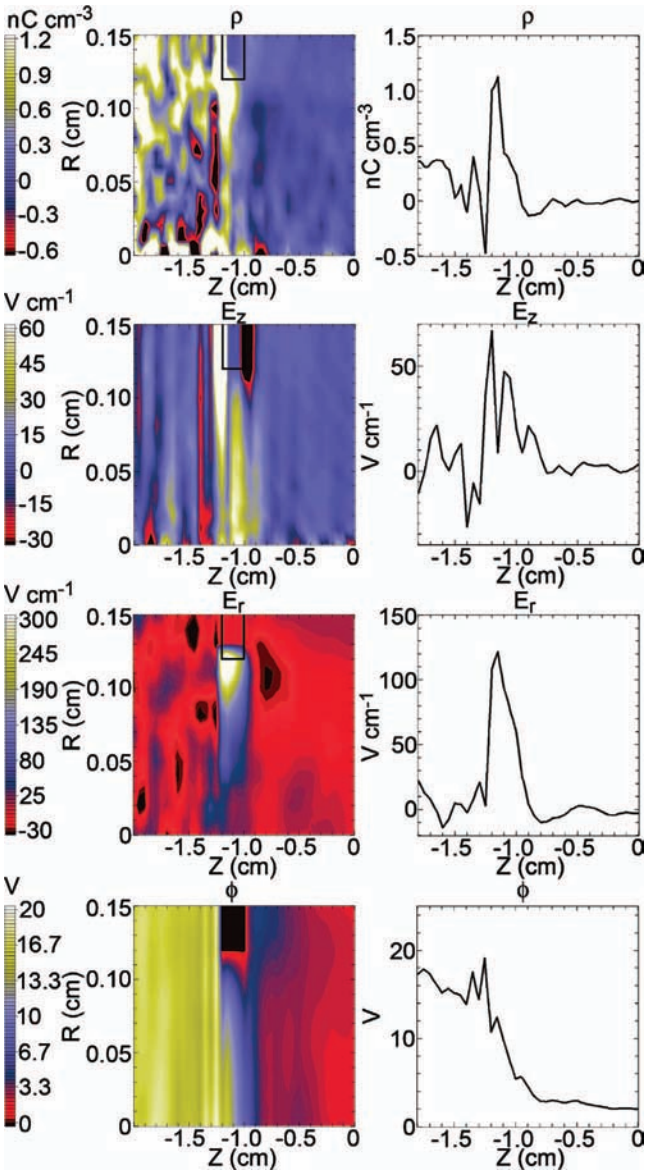

FIG. 7. (Color) $\{r,z\}$ contours (left) and radially averaged axial slices (right) of charge density ρ, axial electric field E_z, radial electric field E_r, and electrostatic potential ϕ. All plots are on a linear scale. The data have been averaged in θ and in time (over $\Delta t \sim +3\ \mu$s during steady state) and are from a lower (by ~ 0.1) plasma density case. White and black regions in the $\{r,z\}$ contour plots contain saturated values above and below the range shown, respectively. The axial slices are radially averaged from $r = 0.01$ cm to $r = 0.11$ cm, and so neglect excess particle noise near the $r \sim 0$ axis as well as the strong sheath fields near the aperture.

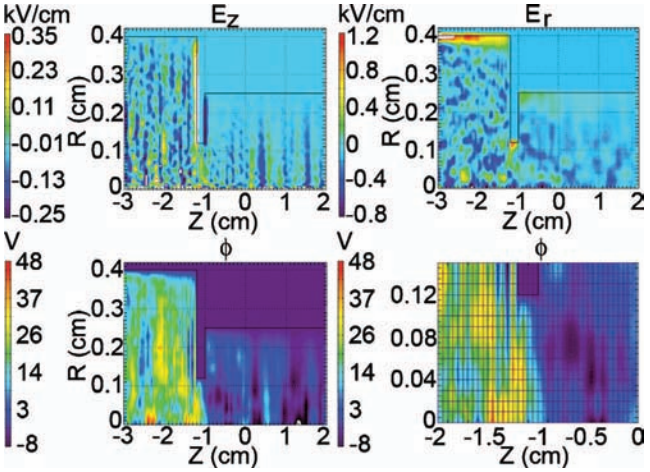

FIG. 8. (Color) Steady-state snapshots of axial electric field E_z (top left), radial electric field E_r (top right), potential ϕ (bottom left), and the same ϕ zoomed near the aperture with the PIC grid overlaid (bottom right), presented as $\{r,z\}$ contours. Coherent waves with $k \| E_z$ are visible.

The DL does not show convergent ion acceleration solutions when the grid spacing within the aperture region has $\Delta z \geq 0.075$ cm (the convergent solutions reported herein use $\Delta z = 0.05$ cm). The axial grid spacings upstream and downstream away from the aperture region show the onset of convergent behavior at larger spacing values. It is not known whether this effect is due to the under-resolution of the aperture itself (and its fields) or of the ion acoustic mode wavelength near the aperture. Ion acoustic DLs have been reported[17,20] to form a dip in ϕ and n_p on the low potential side, and such dips are regularly revealed in MNX simulations and experiments. Some additional discussion on the possible role of IAWs is provided in Sec. V, but detailed quantitative analysis is left for future work.

The noisy effect of the waves on calculating the potential ϕ from the electric field is also evident in Fig. 8. A plot of the same potential values, but zoomed near the aperture and with the underlying PIC grid overlaid, exhibits the level of resolution involved. The potential drop (in $+\hat{z}$) of the DL has 2D structure, and $\phi(r)$ is generally maximum at $r=0$ and decreases with r by a factor of ~ 2 to $r_{\rm ap}$ for the nominal parameters. The 2D structure of the DL's potential arises because of the magnetic field topology and aperture boundary conditions. As reviewed and discussed in Ref. 17, when the perpendicular $+E_r$ fields within the aperture are shorted out outside of the aperture, 2D potential structures are generated with electric fields parallel to the applied magnetic field. As also pointed out in Ref. 17, the generation of this parallel potential drop (E_z) by shorting out the perpendicular (E_r) fields away from their source region (the aperture) is equivalent to applying a potential drop; i.e., a perpendicular potential drop can become a parallel potential drop (the DL) due to boundary conditions and a magnetic field.

Ion kinetic energy profiles $E_i(z)$ that have been averaged in radius and over four consecutive time profiles spaced $\Delta t = +250$ ns apart during steady-state flow are supplied in Fig. 9. The energy corresponding to an argon ion traveling at the sound speed C_s is approximately 3–3.5 eV, a value crossed

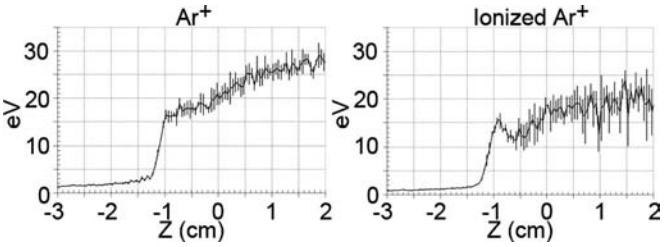

FIG. 9. Steady-state Ar^+ (left) and ionized Ar^+ (right) kinetic energy profiles E_i, averaged in radius and over four consecutive profiles spaced $\Delta t = +250$ ns apart. The error lines are 95% confidence intervals in the mean. The ionized Ar^+ profile in the ER is actually an average of the low-energy ions born there and those accelerated across the DL from the MC.

by the ion beam as it enters the DL within the aperture. The Ar^+ ions are called *supersonic* when their velocities surpass C_s, yielding a Mach number exceeding unity ($M \equiv v/C_s$). The supersonic Ar^+ beam is accelerated across the DL to an energy $\sim 3.4T_e$ (or $M \sim 2.2$) over a distance of $\sim 200\lambda_{D,e} - 300\lambda_{D,e}$, where the Debye length references the T_e and n_e values just *upstream* of the aperture. The ions are accelerated further to an energy $\sim 5.7T_e$ (or $M \sim 2.9$) by $z=+2$ cm, another $\sim 225\lambda_{D,e} - 350\ \lambda_{D,e}$, where the Debye length now references the T_e and n_e values just *downstream* of the aperture, to account for the n_e drop across the DL. Similar to Fig. 6, the energy profile in Fig. 9 of the ionized Ar^+ species in the ER is actually an average of both the low-energy ions born there and those accelerated across the DL. (Recall Fig. 4.)

Now consider the electron distribution differences between the chambers. The average drift velocity for the electrons is $v_e \sim I_e/(en_e \pi r_p^2)$, where r_p is the effective radius ($r_p \sim r_{\rm wall}$ in the MC and $r_p \sim r_{\rm ap}$ in the ER). Recall that n_e and v_e are both functions of z (and r) in the MC and ER, but their product (the flux) at a specific z is separately conserved in both chambers. In fact, the electron flux is also conserved to $\sim 90\% - 95\%$ across the DL, but obviously only for those magnetized particles whose field lines pass through the aperture $r < r_{\rm ap}$. In both the MC and ER, the approximate sound speed range is $C_s/c \sim (1.25-1.4) \times 10^{-5}$. In the MC, the approximate average electron velocity range is $v_e/c \sim (0.5-1.2) \times 10^{-5}$ ($v_e \leq v_i < C_s$); in the ER the range is $v_e/c \sim (0.1-1) \times 10^{-3}$ ($v_e > v_i > C_s$), primarily because of reductions in n_e and r_p, but I_e also decreases (generally, the ranges of C_s, v_e, and v_i are broad because of variations in n_i, n_e, T_i, T_e, and r_p). Thermal electron velocities between 4 and 8 eV are $v_{{\rm th},e}/c \sim (4-5.6) \times 10^{-3}$, and so are substantially greater than the drift speeds v_e or v_i. Therefore, the ions crossing the DL become a supersonic beam in the ER, whereas the electrons in the ER are a thermal population ($v_{{\rm th},e}/v_e \sim 5-50$) but *also* have supersonic average drift speed. Both the ion and electron average drift velocities change from subsonic ($<C_s$) to supersonic ($>C_s$) near the upstream end of the DL within the aperture. Since neither the ion nor electron pressures are conserved across the DL (densities decrease more than the average temperatures increase) and both populations are supersonic in the ER, the electrostatic DL may be considered a stationary shock.

Both the ion energy distribution function (IEDF) and EEDF are displayed in Fig. 10 during steady-state plasma

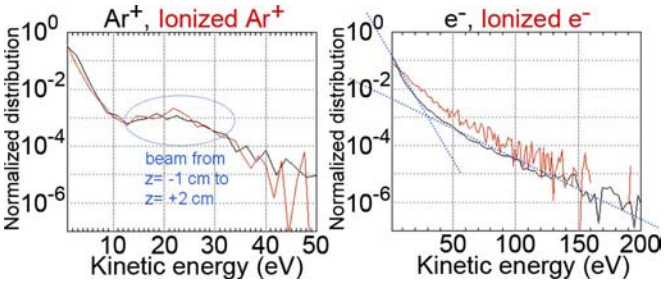

FIG. 10. (Color online) Steady-state ion (left) and electron (right) energy distribution functions over all z for $r<r_{ap}$. Both plots are on a $\log_{10}$ scale. The Ar^+ beam in the ER corresponds to the equally populated circled region from ~15 to 30 eV. Lines with different slopes draw attention to the high-energy tail and two-temperature EEDF created by the DL.

flow over all z for $r<r_{ap}$. The supersonic argon beam in the ER of the MNX device is witnessed within the approximately equally populated ~15–30 eV circled region of the IEDF. The DL is responsible for the generation of a high-energy tail within the EEDF, whose particles are found to mainly exist in the MC. (Recall Fig. 5.) Lines with different slopes on the EEDF in Fig. 10 draw attention to the two-temperature distribution for $r<r_{ap}$, defined as $\text{EEDF}=f_{e,1}\times e^{-E/T_{e,1}}+f_{e,2}\times e^{-E/T_{e,2}}$. The cooler bulk value is bounded by $T_{e,1}\sim 4.8\ \text{eV}\pm 5\%$ and the high-energy tail value is bounded by $T_{e,2}\sim 21.5\ \text{eV}\pm 5\%$; the relative population is bounded by $f_{e,2}/f_{e,1}\sim 2.5\%\pm 0.5\%$. High-energy tails in the EEDF have been measured in the MNX device[9] and are in quantitative agreement. The model excludes the consideration of excited Ar^{+*} states, which may influence the EEDF; excited ions may be included in future work, although their relative population in the MNX is estimated to be low.[21]

It is worth pointing out that the aperture acts as an ion momentum selector, where an upper limit on allowable $v_\perp^2/v_\parallel^2\sim(v_r^2+v_\theta^2)/v_z^2$ exists (relative to the magnetic field) for ions to be able to enter the ER. Figure 11 provides the perpendicular momentum phase space of the ions. If the ions have too much perpendicular momentum and the wrong phase of their gyromotion as they enter the aperture at $r<r_{ap}$, they may strike its interior, magnetic field-parallel wall and be lost. Within the aperture region, the radial and axial electric fields $+E_r$ and $+E_z$ (refer to Figs. 7 and 8) increase

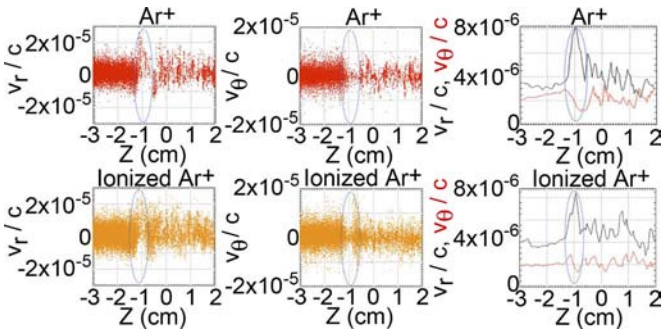

FIG. 11. (Color online) Steady-state $\{z,v_r\}$ (left) and $\{z,v_\theta\}$ (middle) phase space profiles of Ar^+ (top) and ionized Ar^+ (bottom) for $r<r_{ap}$, presented as particle plots. The root-mean-square $v_r(z)$ and $v_\theta(z)$, averaged over $r<r_{ap}$, are also provided (right). The location of the aperture is circled.

the relative $+v_r$ and $+v_z$ distributions, and only ions with small v_θ pass. Notably, the radial ion velocities are generally largest (and almost entirely positive) within the aperture, and a significant fraction of them are supersonic. Conversely, the range of ion v_θ values is smallest at the same location.

The presence of the $+E_r$ sheath field within the aperture is an important contributor to DL formation, as will be discussed in Sec. V. Figure 11 demonstrates that static field significantly affects the trajectories of the ions, since the $+E_r$ extends radially into the entire path of the passing plasma for $r<r_{ap}$ (recall Figs. 7 and 8). The field is perpendicular to the plasma flow, magnetic field, and aperture wall, and its existence is a consequence of the aperture's geometry and boundary conditions. A large amount of plasma flux is lost to the aperture wall at $z=-1.2$ cm for $r>r_{ap}$ in the MC, and the $+E_z$ sheath that develops there is due to differences in electron and ion mobilities. The electric field magnitude is largest near the corner of the aperture on the MC-facing side. The aperture itself is at a lower potential than the plasma, so the $+E_z$ sheath and boundary conditions ensure that the radial E_r field within the aperture has a positive sign. The strength of this $+E_r$ sheath is lower than (and its spatial extent is larger than) a standard sheath because of three contributing factors: (1) the orientation of the magnetic field parallel to the aperture wall at $r=r_{ap}$ creates a magnetized sheath[22] with a characteristic size of the ion Larmor radius $\rho_{L,i}$, (2) the larger $\rho_{L,i}$ (relative to the electron $\rho_{L,e}$) allow proportionally more ion losses to the $r=r_{ap}$ aperture wall, and (3) a larger $\lambda_{D,e}$ because of the lower n_p within the aperture.

Due to the presence of the $+E_r$ sheath field, one may expect to find $E_r\times B_z$ drift motion and witness the Hall effect within the aperture. However, the $\hat{\theta}$ drift motion of the particles is difficult to measure because of particle statistics and the momentum selection process within the aperture. Also, the drift approximation, which underlies the Hall current, loses its applicability because many ions are lost to the aperture before completing even a single gyration. Even so, the presence of some Hall effect is witnessed in plots of $E_\theta(r)$ for various θ at $z=-1.1$ cm (the center of the aperture), which reveals radially constant $E_\theta\sim\pm 25\text{V cm}^{-1}$ values on diametrically opposite sides in θ, implying a Hall voltage ($V_H\sim 12$ V) perpendicular to both the (mostly) axial magnetic field and radial positive current drawn into the aperture.

IV. MNX PARAMETRIC VARIATIONS

An understanding of the overall ion acceleration parameter space available to the MNX device is of primary importance, especially for the advanced spacecraft-propulsion application. Many measurements have been made and reported in the literature regarding parametric variations in the operational setup of the MNX device.[9] An exhaustive simulated parameter scan of all the variables would be an enormous undertaking, given the computational difficulty of these PIC simulations. Variations in a select set of MNX-like conditions are reported here, and the resulting change in the level of ion acceleration produced by the DL is evaluated. In order to help provide insight, only one parameter at a time is changed from the nominal values employed in Sec. II. The

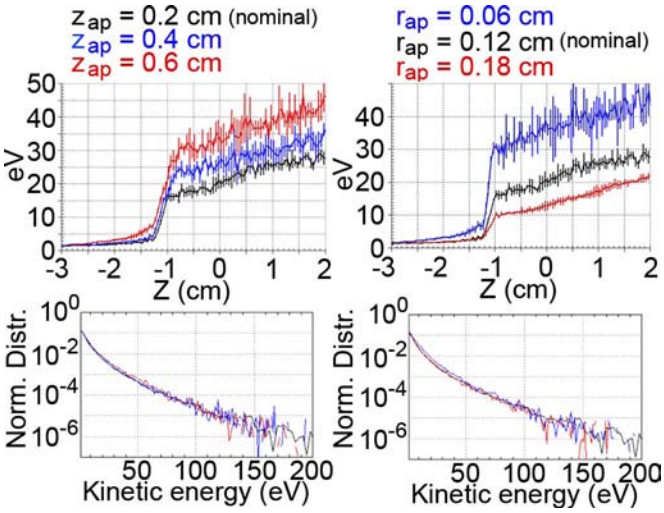

FIG. 12. (Color online) Steady-state Ar^+ kinetic energy profiles E_i (top) for variations in aperture axial length z_{ap} with fixed $r_{ap}=0.12$ cm (left) and aperture radius r_{ap} with fixed $z_{ap}=0.2$ cm (right), averaged in radius and over four consecutive profiles spaced $\Delta t=+250$ ns apart. The error lines are 95% confidence intervals in the mean. Steady-state EEDFs (bottom), over all z for $r<r_{ap}$, and on a $\log_{10}$ scale.

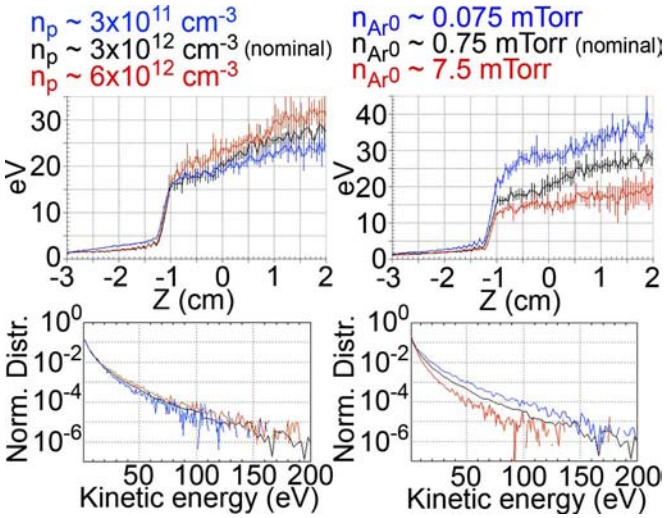

FIG. 13. (Color online) Steady-state Ar^+ kinetic energy profiles E_i (top) for variations in initial injected n_p (left) and background n_{Ar^0} (right), averaged in radius and over four consecutive profiles spaced $\Delta t=+250$ ns apart. The error lines are 95% confidence intervals in the mean. Steady-state EEDFs (bottom), over all z for $r<r_{ap}$, and on a $\log_{10}$ scale.

two figures of merit used to cite quantitative ion acceleration differences between cases are (1) the directed ion energy E_i increase across the DL, called $\Delta\mathcal{E}_i^{DL}$ and measured across the axial extent of the aperture (in the nominal case, $z=-1.2$ cm to $z=-1.0$ cm), and (2) the E_i increase in the ER, called $\Delta\mathcal{E}_i^{ER}$ and measured from the end of the aperture to the end of the simulation in the ER (in the nominal case, $z=-1.2$ cm to $z=+2$ cm). In addition, recall from Sec. III that the EEDF for $r<r_{ap}$ is approximately equal to $f_{e,1}\times e^{-E/T_{e,1}}+f_{e,2}\times e^{-E/T_{e,2}}$, and is well bounded by $\pm 5\%$ in $T_{e,1}$ and $T_{e,2}$ and by $\pm 0.5\%$ in $f_{e,2}/f_{e,1}$. Variations in $T_{e,1}$, $T_{e,2}$, and $f_{e,2}/f_{e,1}$ due to parameter changes are also reported.

First, consider changes in the aperture axial length z_{ap} (by 2 and 3 times) and radius r_{ap} (by 0.5 and 2 times). Figure 12 and Table I summarize the influence of aperture dimensions on the ion acceleration and EEDFs. The directions of the exhibited ion acceleration trends for both variables demonstrate a dependence of DL formation on the plasma interaction with the aperture wall at $r=r_{ap}$. Increasing z_{ap} and decreasing r_{ap} both reveal increases in $\Delta\mathcal{E}_i^{DL}$, $\Delta\mathcal{E}_i^{ER}$, $T_{e,1}$, and $f_{e,2}/f_{e,1}$. Dynamic effects were cited in Sec. II as being able to affect the achieved steady-state equilibrium bulk T_e (also called $T_{e,1}$) for $r<r_{ap}$, and these results show that the DL itself also affects that parameter. A trend in $T_{e,2}$ is not witnessed, since its fit value is bounded by $\pm 5\%$ ($\pm\sim 1$ eV).

Second, consider variations in the injected plasma density n_p (by 0.1 and 2 times) and neutral density n_{Ar^0} (by 0.1 and 10 times). Figure 13 and Table II summarize the resulting changes in ion acceleration and EEDFs. Increasing n_p or decreasing n_{Ar^0} both reveal increases in $\Delta\mathcal{E}_i^{DL}$, $\Delta\mathcal{E}_i^{ER}$, $T_{e,1}$, $T_{e,2}$, and $f_{e,2}/f_{e,1}$. The ion acceleration profile changes imply either a complex, indirect, or weak dependency on n_p (a 20 times increase in n_p results in a $\sim+22\%$ increase in $\Delta\mathcal{E}_i^{DL}$ but an $\sim+65\%$ increase in $\Delta\mathcal{E}_i^{ER}$ and minor changes in the EEDFs). Sheath and DL potentials are expected to be independent of n_p but proportional to T_e. The n_{Ar^0} influences the DL strength and ion acceleration more than changes in n_p because of the affect neutrals have on electron energy lost to ionization (note the changes in steady-state $T_{e,1}$). In the MNX, lower Ar^0 densities are known to exhibit larger bulk T_e values in the MC. A simulated order-of-magnitude decrease/increase in n_{Ar^0} results in an approximate +30%/−30% difference in $(\Delta\mathcal{E}_i^{DL}+\Delta\mathcal{E}_i^{ER})$, respectively. Also, n_p hardly affects the $f_{e,2}/f_{e,1}$, whereas the decrease/increase in n_{Ar^0} significantly affects the superthermal tail by increasing/decreasing both $T_{e,2}$ and $f_{e,2}/f_{e,1}$. Note that the LIF method for measuring ion acceleration in MNX falters at pressures

TABLE I. Comparison of approximate values and best fits. Nominal: $z_{ap}=0.2$ cm and $r_{ap}=0.12$ cm.

Case	$\Delta\mathcal{E}_i^{DL}$ (eV)	$\Delta\mathcal{E}_i^{ER}$ (eV)	$T_{e,1}$ (eV)	$T_{e,2}$ (eV)	$f_{e,2}/f_{e,1}$ (%)
Nominal	11.5	12.2	4.8	21.5	2.6
$z_{ap}=0.4$ cm	13.0	18.8	5.3	20.4	3.5
$z_{ap}=0.6$ cm	16.7	25.0	5.8	19.3	4.7
$r_{ap}=0.06$ cm	23.7	13.8	6.4	18.1	5.2
$r_{ap}=0.18$ cm	6.2	12.3	4.3	19.7	2.2

TABLE II. Comparison of approximate values and best fits. Nominal: $n_p\sim 3\times 10^{12}$ cm^{-3} and $n_{Ar^0}\sim 0.75$ mTorr.

Case	$\Delta\mathcal{E}_i^{DL}$ (eV)	$\Delta\mathcal{E}_i^{ER}$ (eV)	$T_{e,1}$ (eV)	$T_{e,2}$ (eV)	$f_{e,2}/f_{e,1}$ (%)
Nominal	11.5	12.2	4.8	21.5	2.6
$n_p\sim 3\times 10^{11}$ cm^{-3}	9.7	8.8	4.5	17.3	2.4
$n_p\sim 6\times 10^{12}$ cm^{-3}	11.8	14.5	4.9	22.2	2.7
$n_{Ar^0}\sim 0.075$ mTorr	15.3	15.3	7.9	24.8	4.6
$n_{Ar^0}\sim 7.5$ mTorr	9.7	8.1	3.1	12.6	2.4

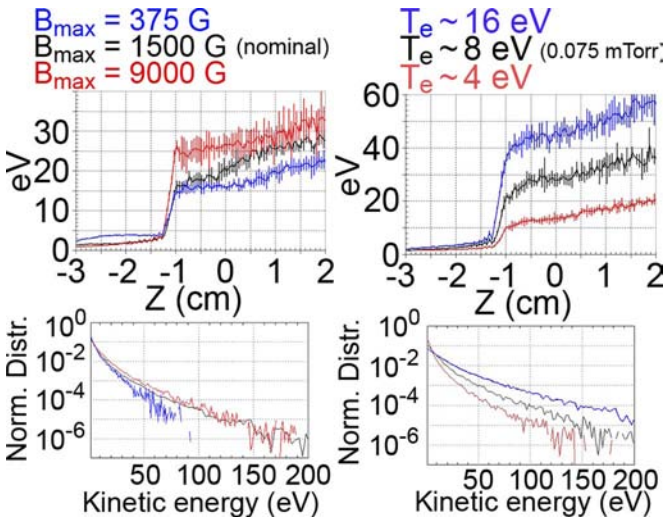

FIG. 14. (Color online) Steady-state Ar^+ kinetic energy profiles E_i (top) for variations in B_{max} (left) and bulk T_e for the $0.1n_{Ar^0}$ case (right), averaged in radius and over four consecutive profiles spaced $\Delta t=+250$ ns apart. The error lines are 95% confidence intervals in the mean. Steady-state EEDFs (bottom), over all z for $r<r_{ap}$, and on a $\log_{10}$ scale.

above 1 mTorr, an effect attributed to collisional quenching of the Ar^{+*} metastable states necessary for LIF.

Third, consider changes in magnetic field magnitude (by 0.25 and 6 times) and steady-state bulk electron temperature $T_{e,1}$ (by 0.5 and 2 times) for $r<r_{ap}$. Figure 14 and Table III summarize the influence of magnetic field and electron temperature on the ion acceleration and EEDFs relative to the nominal case for the variations in B, but relative to the $0.1\ n_{Ar^0}$ case for the variations in T_e (since lower Ar^0 pressure helps reduce ionization effects from varying T_e). Increasing $T_{e,1}$ proportionally increases the strength of the DL and greatly affects the superthermal population due to strengthening of the sheaths near the aperture.

The relation between magnetic field strength and ion acceleration is nuanced. Although larger field magnitudes increase $\Delta\mathcal{E}_i^{DL}$, optimizing the ion acceleration is not just a matter of operating in the high-field limit. As mentioned earlier, no DL forms without an applied field, but it will be argued in Sec. V that the DL vanishes in the strong field or large r_{ap} limits (when $\rho_{L,i}\ll r_{ap}$). The magnetic field directly affects the ion gyroradii and particle flux loss to the aperture at $r=r_{ap}$ but also alters both the n_p and velocity distributions perpendicular ($v_\perp$) and parallel ($v_\parallel$) to the field. The n_p just upstream of the aperture is larger for increased levels of magnetization. Also, the cell temperatures ($kT=2/3\ E_{ave}$) in the MC are "cooler" to "hotter" for smaller to larger field magnitudes, respectively, even though the same injection parameters are used. In the limit of $B\sim 0$, the one-temperature EEDF is recovered and $\Delta\mathcal{E}_i^{DL}$ vanishes; the high value of $f_{e,2}/f_{e,1}$ for the low-field case in Table III is due to this trend ($T_{e,2}$ approaching $T_{e,1}$). The simulations support an intriguing fact that the overall ion acceleration sufficiently downstream of the DL ($\Delta\mathcal{E}_i^{DL}+\Delta\mathcal{E}_i^{ER}$) is only weakly dependent upon the applied field: a 24 times increase in B only yields an $\sim+59\%$ increase in E_i at $\Delta z=+3$ cm from the aperture (or $E_i\sim B^{0.14}$ dependence). The dependency appears to be similarly weak in MNX.[9] However, magnetization reduces radial losses and maintains higher n_p in the chambers, and the DL transports more plasma beyond the aperture. Therefore, the $\rho_{L,i}/\rho_{L,e}$ ratio is posited to be more important to double layer formation.

TABLE III. Comparison of approximate values and best fits. Nominal: $B_{max}=1500$ G. Nominal ($0.1n_{Ar^0}$): $T_e\sim 8$ eV.

Case	$\Delta\mathcal{E}_i^{DL}$ (eV)	$\Delta\mathcal{E}_i^{ER}$ (eV)	$T_{e,1}$ (eV)	$T_{e,2}$ (eV)	$f_{e,2}/f_{e,1}$ (%)
Nominal	11.5	12.2	4.8	21.5	2.6
$B_{max}=375$ G	8.6	8.2	2.9	9.7	11.2
$B_{max}=9000$ G	19.1	7.6	5.7	18.4	6.8
Nominal ($0.1n_{Ar^0}$)	15.3	15.3	7.9	24.8	4.6
$T_e\sim 4$ eV	7.8	10.3	3.8	15.8	2.4
$T_e\sim 16$ eV	30.7	25.9	15.7	39.5	6.2

In summary, when changing one variable at a time from the nominal parameters outlined in Sec. II, stronger DLs (larger potential drops) in the MNX device are associated with (1) longer apertures, (2) smaller aperture radii, (3) increased plasma densities, (4) reduced neutral densities for fixed n_p, (5) increased magnetic field strengths, and (6) increased bulk electron temperatures. The superthermal electron populations in the EEDF are (1) strongly affected by neutral density, magnetic field strength, and bulk electron temperature, (2) modestly affected by plasma density, and (3) not significantly affected by aperture dimensions. Variations in $\Delta\mathcal{E}_i^{DL}$ appear to be correlated most strongly with $T_{e,1}$ compared to $T_{e,2}$. Also note the strong correlation between $\Delta\mathcal{E}_i^{DL}$ and $f_{e,2}/f_{e,1}$, which share a consistent trend in all cases.

V. DISCUSSION OF DOUBLE LAYER FORMATION

The simulations presented in the previous sections provide insight into the formation mechanism of the DL in the MNX device. As already mentioned, the creation of a DL requires both an aperture and imposed magnetic field topology, mostly perpendicular to the MC-facing aperture wall. Accordingly, the formation mechanism must be related to the interaction between magnetized plasma flow and the obstructing object. When one compares the ion energy $E_i(z)$ profiles (e.g., Fig. 9) with the ion density $n_i(z)$ profiles (e.g., Fig. 3), the axially directed ion particle flux $\Gamma_i(z)\sim n_i(z)v_z(z)$ is revealed to be approximately conserved in the MC and the ER separately, but *not* across the aperture. Changes in $E_i(z)$ and $n_i(z)$ in the separate chambers can be explained by particle flux conservation along the magnetic field but *not* within the DL, where ions are preferentially lost to the wall at $r=r_{ap}$. Radial ion losses to the outermost walls in both chambers cause minor deviations from precise flux conservation. One longer simulation extending to $z=+10$ cm confirms continued acceleration of ions into the ER approximately consistent with flux conservation and plasma expansion along a diverging field.

Importantly, the simulations show a correlation between the amount of ion flux transmission through the aperture,

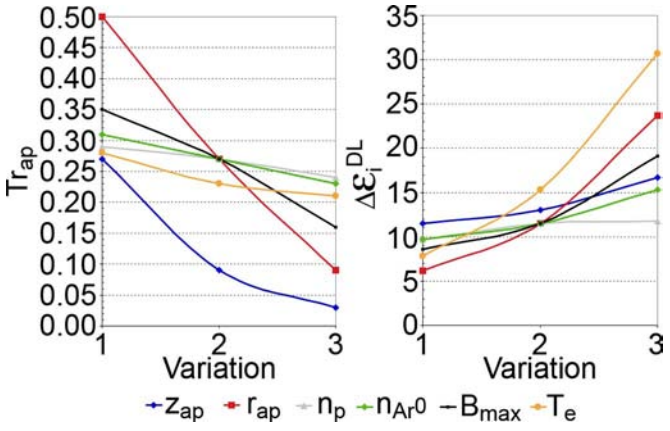

FIG. 15. (Color online) Ion flux transmission $Tr_{\rm ap}$ through the aperture (left) and the ion energy gain $\Delta\mathcal{E}_i^{\rm DL}$ across the aperture (right). Variations {1,2,3} correspond to the cases $z_{\rm ap}=\{0.2,0.4,0.6\}$ cm, $r_{\rm ap}=\{0.06,0.12,0.18\}$ cm, $n_p=\{3\times10^{11},3\times10^{12},6\times10^{12}\}$ cm^{-3}, $n_{\rm Ar0}=\{0.075,0.75,7.5\}$ mTorr, $B_{\rm max}=\{375,1500,9000\}$ G, and $T_e=\{4,8,16\}$ eV (at $0.1n_{\rm Ar0}$ of nominal).

called $Tr_{\rm ap}$, and the amount of ion acceleration across the aperture: smaller values of $Tr_{\rm ap}$ correspond to larger values of $\Delta\mathcal{E}_i^{\rm DL}$, as shown in Fig. 15 for all the parametric variations presented in Sec. IV. The quantity $Tr_{\rm ap}$ is measured in steady state by evaluating the average n_i (over $r<r_{\rm ap}$ and θ) and average v_i (from E_i in Figs. 12–14) at the upstream and downstream ends of the aperture for each of the cases, and then evaluating the ratio of their products between the chambers. As defined in Sec. IV, the quantity $\Delta\mathcal{E}_i^{\rm DL}$ is also a comparison of values between the upstream and downstream ends of the aperture, where most of the ion acceleration takes place (although the DL is generally longer than $z_{\rm ap}$).

Ion flux transmission through the aperture can vary from ~3%–50% for the parameters considered here, as illustrated in Fig. 15. However, electron flux transmissions are typically ~90%–95%, since the electrons are heavily magnetized (although n_e and n_i both decrease across the DL, only the average electron drift velocity v_e increases by a comparable amount, not the average v_i). Three contributing factors to the preferential ion flux loss within the aperture are (1) the difference in ion and electron Larmor radii ($\rho_{L,i}/\rho_{L,e}\sim55$ assuming $T_{\perp,i}\sim0.3$ eV, $T_{\perp,e}\sim5$ eV, and $v_\perp\sim v_{\rm th}$), (2) the fact that $\rho_{L,i}\sim r_{\rm ap}$ [~0.3 cm (at $B_z\sim1500$ G) and 0.12 cm, respectively], and (3) the strong and extended $+E_r$ sheath field within the aperture that increases positive radial current. In fact, the $+E_r$ field serves to help *funnel* electrons through the aperture and toward the $r=0$ axis.

The fact that the DL strength increases with decreasing ion flux transmission $Tr_{\rm ap}$ is not surprising. The strength of an ordinary sheath scales as $T_e\ln(m_i/m_e)$. The $\ln(m_i/m_e)$ term comes from the ratio of ion to electron speeds (i.e., fluxes). More massive ions are slower, so the sheath strength increases to repel more electrons and balance the fluxes. Radial ion losses in the aperture reduce the effective ion mobility relative to the electrons in a way similar to higher masses reducing the ion flux, resulting in a higher DL potential (confirmed by varying m_i in simulations).

The formation of the DL in the MNX device is argued to occur as follows. In the first few microseconds of a simulation or experiment, the plasma expands from the MC toward the ER. The expanding front is not charge neutral; electrons have T_e and higher mobility, causing them to move ahead of the ions and create an expansion $+E_z$ sheath (due to separated charge density regions) at the edge of the plasma (and along the magnetic field), which leads to the initial plasma movement away from the source region. In simulations, the E_z sheath naturally appears and is readily diagnosed.

When plasma flow along the magnetic field (with $\rho_{L,e}\ll\rho_{L,i}\sim r_{\rm ap}$) encounters the aperture between the MC and ER, ions are preferentially lost to its wall at $r=r_{\rm ap}$, as previously mentioned. The $\phi(z)$, $n_e(z)$, and $n_i(z)$ drops of the DL between the MC and ER are evident in simulations as soon as the initial plasma expansion encounters the obstruction, and the relative drops continue to grow as density builds in the MC. Ion flux is lost as a function of whether particle trajectories encounter $r=r_{\rm ap}$ along $z_{\rm ap}$, and the $+E_r$ sheath within the aperture strongly influences the likelihood of wall impact; Fig. 15 shows that the majority of ions are generally lost, so that ion particle flux is rapidly reduced whereas electron flux is not (magnetization and the $+E_r$ help keep electron transmission high). Since the electrons are able to pass the aperture easily, they continue to facilitate the acceleration of ions through it in a completely analogous fashion as the initial expansion. Electrons accumulate on the downstream end of the aperture and maintain a region of ρ^- in an attempt to increase the forward ion flux and plasma expansion.

The DL is therefore seeded from the initial $+E_z$ expansion front. In effect, the region of excess n_i, which normally lags the region of excess n_e in the expansion front (and reaches it at a boundary away from the source, creating a wall sheath), is not able to effectively penetrate the aperture because of the magnetic field and the aperture's boundary conditions. This explanation is very similar to the one cited in Ref. 23, wherein DL formation is stated to occur due to a dramatic change in boundary conditions and not solely as a result of a magnetic nozzle. Likewise, the preferential ion loss in MNX from $\rho_{L,e}\ll\rho_{L,i}\sim r_{\rm ap}$ is not directly due to whether the magnetic topology converges, diverges, or is constant. The strength of the current-carrying DL grows in response to the increasing preferential loss of ion flux [from $n_i(t)$ growing in the MC] until steady-state flow is achieved. These early-time processes occur on too short a time scale (and with too small fields and densities) to be accurately resolved in the MNX at this time, but some were seen in experiments of higher density expanding plasma.[23–26]

The description of currents within the circuit, which includes the MC, aperture, DL, and ER, is complex and 2D in nature. History probes measure the ion I_i, electron I_e, and total I_t (I_i+I_e) currents through axial planes upstream, within, and downstream of the aperture for either $r\le r_{\rm ap}$ or all r. The difference in ion and electron magnetization levels within the nozzle-like field implies that the radial current components of each may change separately as a function of space. The probes measure only axial current and neglect radial components, which are especially important for $r<r_{\rm ap}$ near $z\sim-1.2$ cm.

The normalized axial $I_i(z)$ for $r\le r_{\rm ap}$ within the aperture for the nominal case is provided in Fig. 16. The plot shows

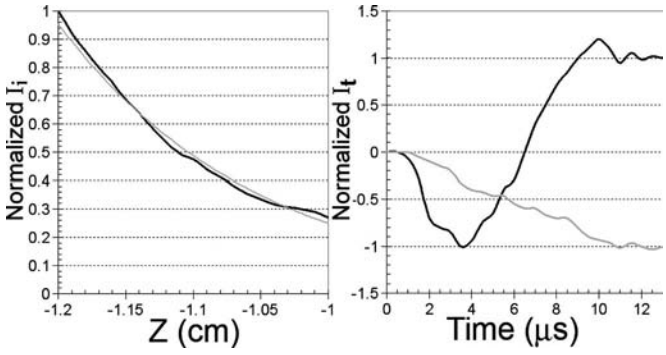

FIG. 16. Steady-state normalized ion axial current $I_i(z)$ (black) and exponential fit (gray) for $r \leq r_{ap}$ within the aperture (left), and normalized total axial current $I_t(t)$ (right) over all r at $z=-1.2$ cm (black) and $z=-1.0$ cm (gray). The nominal case data have been averaged to reduce fluctuations. The two normalization factors are not the same [so that $I_i(z)$ decreases from 1 to $Tr_{ap} \sim 0.27$], and radial currents are neglected.

an approximately exponential decrease in $+I_i(z)$ with z, in corroborating support of the exponential trend of Tr_{ap} with z_{ap} (refer to Fig. 15); it also reveals ion flux loss within the aperture from 1 to the nominal case value $Tr_{ap} \sim 0.27$. In contrast, the negative $I_e(z)$ only increases $<10\%$ within the aperture, the majority of which occurs on the upstream end. Within the defined aperture boundaries, $I_t(z)<0$ and becomes more negative with z due primarily to the decrease in $+I_i(z)$. Therefore, considering only the aperture region $\Delta z = z_{ap}$ for $r \leq r_{ap}$, the DL carries a negative axial current (unneutralized $+\hat{z}$-moving I_e, as explained earlier). However, the DL also carries substantial positive radial current, which the axial probes do not reveal. Also recall that the DL is actually longer than the length z_{ap}, and the currents are inherently 2D because of the boundary conditions and magnetic field. The $I_t(z)$ becomes positive within (or just upstream of) the DL at some $z<-1.2$ cm [when collecting $r \leq r(z)$, where $r(z)$ mimics the shape of a field line and decreases with z to $r(z)=r_{ap}$ at $z=-1.2$ cm], which implies a narrow region within (or near the beginning of) the DL where $I_t \sim 0$.

The normalized axial $I_t(t)$ over all r through the planes $z=-1.2$ cm and $z=-1.0$ cm in the MC and ER, respectively, are also shown in Fig. 16. The currents are normalized to the steady-state value of I_t (~ 5 mA in the nominal case), where steady-state flow exists for approximately $t \geq \sim 11$ μs in the nominal case shown. In steady state, $I_t=+1$ at $z=-1.2$ cm due to a 5:4 proportion of $I_i:I_e$; approximately the same I_t is measured in the MC by probes located at $z \leq -1.2$ cm (over all r) because of flux conservation. In steady state, $I_t=-1$ at $z=-1.0$ cm due to a 0.15:1.15 proportion of $I_i:I_e$; again, approximately the same I_t is measured in the ER by probes located at $z \geq -1.0$ cm. Note that these probes include $r > r_{ap}$ current contributions, which may be present in the MC but are negligible in the ER.

The pre-steady-state behavior of $I_t(t)$ in Fig. 16 is explained as follows. Early in time, I_t in the MC is negative and decreases because of the initial expansion caused by the electron-rich sheath. The I_t in the MC then increases as both the ion density and the aperture's presheath strength build, and the Bohm criterion is satisfied. Recall that the DL starts forming early, and reflected and accelerated I_e from the DL contributes to the increasing I_t in the MC. Unlike the MC situation, I_t in the ER only monotonically decreases from zero until steady state. The trailing ion flux of the initial expansion never matches the electron flux in the ER because of ion losses in the aperture; the ER plasma is "stuck" in an expanding mode to increase $+\hat{z}$ ion flux. Notice that the minimum I_t in the MC (-1 at $t \sim 4$ μs) is the same magnitude as the I_t reached in the ER at steady state.

The forms of $I_t(t)$ in the MC and ER are the same in the parameter variation cases of Sec. IV, with minor differences. The flux normalization factors change in expected ways (e.g., currents are larger in the higher n_p case). The positive overshoot ($>+1$) in the MC signal just before the onset of steady state is also present in the other cases and is thought to be related to a feedback response leading to steady state (such as when the MC density stops growing). For reference, 11 $\mu s \sim 4$ cm$/C_s$, the simulated MC has $\Delta z \sim 2$ cm, and so steady state begins around the time required for information traveling at $v=C_s$ to cross the MC and back (and is also close to the time required to cross the entire simulated Δz).

During steady state in the MC, the ion component of I_t is $I_i \sim 20-30$ mA (over all r) in the nominal case and is roughly equal to the ion saturation current $I_{sat} \sim n_e C_s e A$. Since I_e is also near I_i (closer if one neglects the reflected/accelerated contribution), the average electron (drift) velocity in the MC can approach $v_e \sim C_s$ in the laboratory frame but not in the ion frame. This fact and the facts that $v_e \leq v_i < C_s$ in the MC but $v_e > v_i > C_s$ in the ER (meaning both sets of distributions share the same sign of df/dv at $v=v_{ph} = \omega/k \sim C_s$) imply that the IAWs may be electron current-driven *stable* in both chambers separately; wave-particle instability requires $v_i < C_s < v_e$ so that the ion and electron distributions have the opposite df/dv sign at $v=v_{ph}$.

However, the analysis of the electron current-driven IAW instability is more complicated in MNX. The growth rate has a stabilizing ion term that is small when $T_i \gg T_e$ and a destabilizing electron term requiring $v_e > C_s$,[18] which is solidly true in the ER, and perhaps also satisfied (marginally or not) in the vicinity of the DL. The usual IAW analysis is done in the ion frame, where $v_i < C_s$ is true in the MC but also true for the ionized ions in the ER, and does not consider the possible influence of a complex EEDF. In addition, the subsonic to supersonic transition caused by the DL for both species near the upstream end of the aperture does not preclude the possibility that $v_i < C_s < v_e$ may be satisfied in that vicinity. For example, the $-E_z$ and ρ^--rich region near -1.45 cm $> z > -1.25$ cm (refer to Fig. 7) may provide sufficient downstream electron acceleration (and ion deceleration) to provide $v_e > C_s$ (and $v_i < C_s$). Also, neglecting the reflected/accelerated electron contribution to I_e increases the calculated v_e. Therefore, the possibility exists that the IAW mode exists throughout MNX but is *unstable* both (1) just upstream of the aperture in the MC and (2) in the ER because of ionized ions and supersonic electrons.

Why the IAW mode appears to thrive in density, field, and particle plots of MNX simulations (even though $T_i/T_e \sim 0.05-0.15$ implies ion Landau damping) and whether it is stable or unstable to electron current-drive [because of T_i/T_e

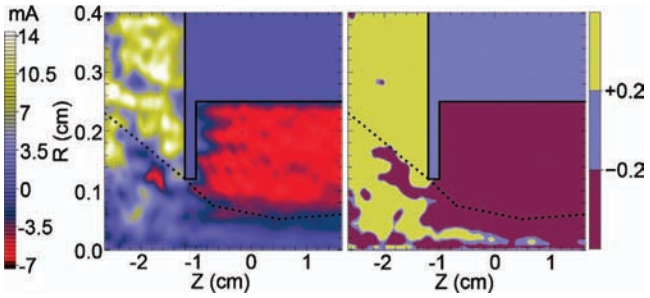

FIG. 17. (Color) $\{r,z\}$ contour of rB_θ values showing the enclosed $I_t(r)$ distribution in the nominal case (left), and the same data on a reduced scale to show $\{+,\sim 0,-\}$ signals (right), on a linear scale. The values have been averaged in θ and in time (over $\Delta t \sim +3$ μs during steady state), as well as boxcar averaged in r and z. The dotted line approximates the outer radius enclosing most of the $I_t(r,z)$.

(stability) and $v_i < C_s < v_e$ (instability)] are presently unresolved. The IAWs may actually be simultaneously unstable (electrons give energy to IAWs) and ion Landau damping (IAWs give energy to ions). The wavelike modulation in E_i witnessed just upstream of the aperture may be due to such an interaction (refer to Fig. 9 and note that the error bars are much smaller than the amplitude of the E_i modulation). Furthermore, any interplay between IAW stability and instability may be influenced by the DL, which generates both upstream-moving superthermals and downstream-moving supersonic v_e, and could be related to the onset of steady state (and a feedback mechanism between the chambers).

A plot of rB_θ [enclosed $I_t(r)$] during steady-state flow is given in Fig. 17 in order to illustrate the 2D nature of the current distribution (a reduced scale plot is also provided to show $\{+,\sim 0,-\}$ signals more clearly). The values have been averaged in θ and in time (over $\Delta t \sim +3$ μs during steady state), as well as boxcar averaged in r and z, to reduce fluctuations from waves and particle noise.

Figure 17 directly reveals that most of the total current passes through the aperture approximately along field lines. The dotted line approximates the outer radius enclosing most of the $I_t(r,z)$, and also roughly follows a field line that intersects the aperture (the outermost path an electron that encounters the DL could follow). Above the line, the enclosed I_t is positive in the MC and negative in the ER, as described earlier. Since the values above the line are approximately constant in both chambers (rather than, say, linearly increasing with r), the majority of the I_t is within the field lines that pass through the aperture. The contribution above the dotted line in the MC may be small because, although ion and electron currents exist there, the fluxes to the aperture at $r > r_{ap}$ are about equal; there is almost no contribution above the line in the ER because of the shadow of the aperture.

An extended region of negative enclosed I_t upstream of the aperture and near the dotted line persists after the spatial and temporal averaging of the data (the most negative region is near the corner of the aperture, where the E field magnitude is largest and repels electrons). Notably, the rB_θ plot clearly shows the $-\hat{r}$-directed funneling effect the $+E_r$ sheath field within the aperture has on the electrons as they drift in $+\hat{z}$. A thin region of positive I_t extending into the ER near $r \sim 0$ is apparent, and may be related to the ionized species preferentially born there (due to funneled electrons).

The reduced scale plot of Fig. 17 demonstrates that the region within the defined aperture boundaries has $I_t(z) < 0$ on average (as does some of the surrounding region), as mentioned earlier. However, the rB_θ plot roughly shows that a step occurs near $z \sim -1.2$ cm at $r \sim r_{ap} + 0.02$ cm, while one also occurs near $z \sim -1.0$ cm at $r \sim r_{ap} - 0.02$ cm. The DL actually has radial structure and axially extends beyond the aperture boundaries (approximately bounded by -1.4 cm $\leq z \leq -0.8$ cm, or $\Delta z^{DL} \leq 0.6$ cm); $I_t(z)$ becomes positive when rB_θ is measured just $\Delta z \sim 0.1-0.2$ cm upstream of the aperture with slightly larger r. The DL itself is concluded to have a small, nearly current-free ($I_t \sim 0$) location within (as does the aperture and DL circuit when I_t over all r is considered between the MC and ER), but current exists throughout the rest of its extent. The entire circuit is a current-carrying 2D object because of the magnetized aperture boundary conditions that give rise to the double layer.

VI. SUMMARY AND FUTURE WORK

Significant ion acceleration from a double layer is witnessed in detailed PIC simulations of the MNX device, which include the realistic plasma and ionization parameters, magnetic topology, and mechanical aperture. The simulations agree with MNX data,[9] particularly in terms of (1) the spatial extent of the DL, which is $\sim 200\lambda_{D,e} - 300\lambda_{D,e}$ [established by the aperture boundary conditions, and larger than many other DLs reported ($\sim 50\lambda_{D,e}$)], (2) the amount and spatial dependence of ion acceleration, (3) the plasma density $n_p(z)$ and potential $\phi(z)$ drops near the aperture, and (4) the two-temperature EEDF (generation of a high-energy tail).

The 2D electrostatic double layer, composed of distinct axially separated ρ^+ and ρ^- charge density regions, is responsible for generating a supersonic ion beam in the ER; the average drift velocity of the electrons is also supersonic there. A superthermal electron population is measured in the MC because the DL accelerates those species from the ER into the MC, wherein the two-temperature EEDF cools out of an initially hotter one-temperature Maxwellian injected from the boundary, not as a result of heating (or Maxwell's demon). The bulk electrons play the dominant role in determining the strength of the DL.

The double layer formation is intimately related to magnetized plasma interaction with the boundary conditions of the aperture. The DL is seeded by the initial expansion $+E_z$ sheath when it encounters the aperture, and charge separation is maintained within because of preferential ion losses due to $\rho_{L,e} \ll \rho_{L,i} \sim r_{ap}$. The DL carries a small net negative current within the defined aperture region, and its strength grows to a steady-state condition, maintained by various plasma and system parameters which affect sheath physics, in order to maximize forward ion flux into the ER. Lower ion transmissions through the aperture are directly correlated with stronger DLs, whereas electron transmission through the aperture is high. Analogous dynamic DL structures located at an ion-rich expansion front (where the expansion $+E_z$ field is also located) have also been analyzed[27] in the context of ion ac-

celeration during thin-foil plasma expansion after heating by an ultrashort laser pulse (note that two-temperature EEDFs are also reported and discussed in Ref. 27).

Ultimately, the source of the double layer's formation energy is the electron T_e provided by the rf helicon source. Although neutrals are experimentally necessary for plasma production, their inclusion in the model is not necessary to form a DL, so long as plasma is (artificially) injected; on the contrary, the DL model and experiments[28] in an expanding magnetic field and chamber require additional upstream ionization of neutrals by accelerated electrons in order to balance particle losses. A DL does not develop in MNX if there is no magnetized plasma-wall interaction, i.e., a situation of (1) applied magnetic field with no aperture, (2) aperture with no field (also, the DL strength weakens as the field is reduced), or (3) $\rho_{L,e}, \rho_{L,i} \ll r_{\mathrm{ap}}$. Therefore, DL formation is bounded in both the low- and high-field limits so $\rho_{L,e} \ll \rho_{L,i} \sim r_{\mathrm{ap}}$ is satisfied; such a condition is contrary to the observations[29] in an expanding plasma and chamber that only a low-field limit exists, which those authors speculated corresponds to $\rho_{L,i} \leq r_{\mathrm{chamber}}$ and the *reduction* of radial ion losses to a boundary. Finally, note that this model does not require the magnetic field to be converging or diverging, as in other models of DL formation in helicon experiments.

A number of outstanding questions and areas for further work are envisioned but left for future publications: (1) additional parameter scans of system and plasma variables (higher n_p, aperture locations, non-radially constant injected plasma profiles, m_i and T_i changes, applied field topologies, biased walls, etc.); (2) detailed quantitative comparisons to experimental data; (3) discussions of 3D effects (including the Hall effect); (4) consideration of a Child–Langmuir-like theory for DL strength based on ion transmission, where reduced transmission acts like increased ion mass; (5) studies of helicon wave interaction and breakdown in the source region in order to determine whether superthermal electron generation occurs there and influences the DL; (6) thorough ion acoustic wave analysis (theoretical, numerical, and experimental), including whether the IAWs are unstably driven near the aperture (where $v_i < C_s < v_e$ is possible) and provide energy to ions via Landau damping; (7) an investigation of two-stream instabilities; (8) an adequate understanding of radial density and temperature dips and peaks on axis both in the injected and ionized populations, and how they relate to neutralization processes; (9) an investigation of excited Ar^{+*} states and charge-exchange processes, which may influence the EEDF (although the relative population of excited states is estimated to be small and the mean free path for charge exchange is estimated to be 100 cm); and (10) further evaluation of whether the wavelike E_i modulations, negative charge layer, and $-E_z$ that exist just upstream of the dominant DL feature indicate the existence of IAW instability and damping, another weaker DL (forming a quadruple layer), or multiple layers of varying strength.

Although we have demonstrated several ways to increase the specific impulse of the accelerated ions, these methods are costly in terms of energy expended and particles lost. Hence, implementing a grid of apertures might not be suitable for spacecraft propulsion, wherein fuel utilization and energy efficiency are of paramount importance. The ion acceleration method proposed by Chang-Diaz,[3] ion cyclotron resonant heating, should be analyzed by these PIC methods, along with the important question of plasma detachment from the magnetic field.

ACKNOWLEDGMENTS

Sandia is a multiprogram laboratory operated by Sandia Corporation, a Lockheed Martin Company, for the United States Department of Energy's National Nuclear Security Administration under Contract No. DE-AC04-94AL85000. This work was supported in part through the Princeton Plasma Physics Laboratory by the United States Department of Energy Contract No. DE-AC02-76-CHO-3073. The authors would like to acknowledge R. C. Davidson, M. C. Herrmann, and E. Scime for support, X. Sun and A. Keesee for experimental work, I. D. Kaganovich for helpful feedback and suggestions, and D. R. Welch for LSP code information.

[1] S. A. Cohen, N. S. Siefert, S. Stange, R. F. Bolvin, E. E. Scime, and F. M. Levinton, Phys. Plasmas **10**, 2593 (2003).
[2] C. Charles and R. W. Boswell, Appl. Phys. Lett. **82**, 1356 (2003).
[3] F. R. Chang-Diaz, Sci. Am. **283**(5), 90 (2000).
[4] X. Sun, C. Biloiu, R. Hardin, and E. E. Scime, Plasma Sources Sci. Technol. **13**, 359 (2004).
[5] A. Meige, R. W. Boswell, C. Charles, and M. M. Turner, Phys. Plasmas **12**, 052317 (2005).
[6] F. F. Chen, Phys. Plasmas **13**, 034502 (2006).
[7] M. A. Lieberman and C. Charles, Phys. Rev. Lett. **97**, 045003 (2006).
[8] A. Fruchtman, Phys. Rev. Lett. **96**, 065002 (2006).
[9] S. A. Cohen, X. Sun, N. M. Ferraro, E. E. Scime, M. Miah, S. Stange, N. S. Siefert, and R. F. Bolvin, IEEE Trans. Plasma Sci. **34**, 792 (2006).
[10] C. K. Birdsall and A. B. Langdon, *Plasma Physics via Computer Simulation* (McGraw-Hill, New York, 1985).
[11] LSP is a software product developed by ATK Mission Research, Albuquerque, NM 87110, with initial support from the Department of Energy SBIR Program.
[12] T. P. Hughes, S. S. Yu, and R. E. Clark, Phys. Rev. ST Accel. Beams **2**, 110401 (1999).
[13] M. Reiser, *Theory and Design of Charged Particle Beams* (Wiley, New York, 1994), Sec. 3.3.1, p. 66.
[14] D. R. Welch, D. V. Rose, R. E. Clark, T. C. Genoni, and T. P. Hughes, Comput. Phys. Commun. **164**, 183 (2004).
[15] D. R. Welch, T. C. Genoni, R. E. Clark, and D. V. Rose, J. Comput. Phys. **227**, 143 (2007).
[16] X. Sun, A. M. Keesee, C. Biloiu, E. E. Scime, A. Meige, C. Charles, and R. W. Boswell, Phys. Rev. Lett. **95**, 025004 (2005).
[17] N. Singh, H. Thiemann, and R. W. Schunk, Laser Part. Beams **5**, 233 (1987).
[18] R. J. Goldston and P. H. Rutherford, *Introduction to Plasma Physics* (Institute of Physics, Bristol, 1995), Sec. 5, Chap. 25, p. 429.
[19] T. Sato and H. Okuda, Phys. Rev. Lett. **44**, 740 (1980).
[20] T. Sato and H. Okuda, J. Geophys. Res. **86**, 3357, DOI: 10.1029/JA086iA05p03357 (1981).
[21] A. M. Keesee, personal communication (Oct. 31, 2007).
[22] N. Sternberg and J. Poggie, IEEE Trans. Plasma Sci. **32**, 2217 (2004).
[23] H. S. Byhring, C. Charles, A. Fredriksen, and R. W. Boswell, Phys. Plasmas **15**, 102113 (2008).
[24] C. Charles and R. W. Boswell, Phys. Plasmas **11**, 3808 (2004).
[25] G. Hairapetian and R. L. Stenzel, Phys. Rev. Lett. **61**, 1607 (1988).
[26] C. Biloiu, X. Sun, E. Choueiri, F. Doss, E. Scime, J. Heard, R. Spektor, and D. Ventura, Plasma Sources Sci. Technol. **14**, 766 (2005).
[27] P. Mora, Phys. Rev. E **72**, 056401 (2005).
[28] S. Chakraborty Thakur, Z. Harvey, I. A. Biloiu, A. Hansen, R. A. Hardin, W. S. Przybysz, and E. E. Scime, Phys. Rev. Lett. **102**, 035004 (2009).
[29] C. Charles and R. W. Boswell, Appl. Phys. Lett. **91**, 201505 (2007).